

## Pressure-Induced Ferroelastic Transition Drives a Large Shape Change in a Ni(II) Complex Single Crystal

Boyang Fu, Ying Zhao, Yu Liu, Weilong He, Fuyang Liu, Dongzhou Zhang, Luhong Wang, Haozhe Liu, Wei Li,\* and Weizhao Cai\*



Cite This: *J. Phys. Chem. Lett.* 2023, 14, 3891–3897



Read Online

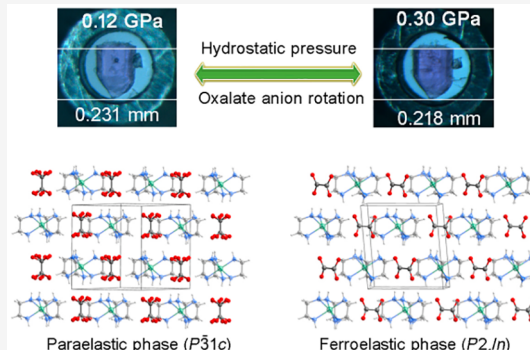
ACCESS |

Metrics & More

Article Recommendations

Supporting Information

**ABSTRACT:** Crystals with significant length reduction at an accessible low pressure are highly desirable for piezo-responsive devices. Here, we show a molecular crystal  $[\text{Ni}(\text{en})_3](\text{ox})$  ( $\text{en}$  = ethylenediamine and  $\text{ox}$  = oxalate anion) that exhibits an abrupt shape change with a contraction rate of  $\sim 4.7\%$  along its  $c$  axis near the phase transition pressure of  $\sim 0.2$  GPa. High-pressure single-crystal X-ray diffraction and Raman spectroscopy measurements reveal that this material undergoes a first-order ferroelastic transition from high-symmetry trigonal  $P\bar{3}1c$  to low-symmetry monoclinic  $P2_1/n$  at  $\sim 0.2$  GPa. The oxalate anions serve as unique components, and their disorder–order transformation and rotation of  $90^\circ$  through cooperative intermolecular hydrogen bonding triggered unconventional anisotropic microsize contraction under compression, which can be appreciated visually. Such a prominent directional deformation at a low pressure driven by molecular motors of oxalate anions provides insights for the design of novel molecular crystal-based piezo-responsive switches and actuators in deep-sea environments.



Materials with ferroelastic transition generally undergo a change of point group with symmetry breaking and demonstrate nonlinear elastic hysteresis of strain.<sup>1</sup> As a mechanical analog of ferromagnetism and ferroelectricity, ferroelasticity features two or more switchable orientation states of spontaneous lattice strain and plays a key role in actuators, piezoelectric sensors, and mechanical switches.<sup>2–4</sup> Most ferroelastic materials exhibit phase transitions between a low-symmetry ferroelastic phase and a high-symmetry paraelectric phase, and it is the most common characteristic of natural materials (e.g., oxides and minerals) in the Earth's crust and mantle.<sup>5</sup> For example, the mineral paratellurite  $\text{TeO}_2$  adopts a distorted rutile structure with  $P4_{1}2_{1}2$  symmetry, and a continuous ferroelastic transition (second-order nature) occurs at  $\sim 0.9$  GPa (to an orthorhombic  $\text{CaCl}_2$ -type structure) with an expansion of the  $b$  axis (i.e., negative linear compressibility).<sup>6–8</sup> In contrast, the prototypic material, lead phosphate  $\text{Pb}_3(\text{PO}_4)_2$ , undergoes a reverse (improper) ferroelastic transition: the low-symmetry monoclinic phase transforming to a rhombohedral phase at  $\sim 1.8$  GPa involves disordering of the displacement of  $\text{Pb}$  sites and correlated tilt of  $\text{PO}_4$  tetrahedra.<sup>9,10</sup>

Ferroelasticity has also been found in a large number of hybrid organic–inorganic materials with changes in the temperature.<sup>11–18</sup> The high-symmetry phase converts to the low-symmetry phase with symmetry-breaking upon cooling, and disordered cations are conventionally frozen at low temperatures; thereby, disorder–order transformation occurs during the phase transition.<sup>19–21</sup> Meanwhile, the molecules within the

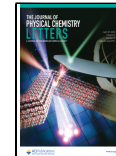
crystals may undergo displacement and rotational motion, resembling that of inorganic ferroelastics.<sup>22</sup> For example, a hybrid material  $(\text{Me}_3\text{NOH})_2[\text{ZnCl}_4]$  undergoes a ferroelastic transition at 373 K with symmetry change of  $P2_1/n \rightarrow Pnma$ , and the cooperation of the order–disorder transition of the  $(\text{Me}_3\text{NOH})^+$  cation and intermolecular interactions resulted in large spontaneous strain.<sup>23</sup> In these types of materials, all studies have been performed with the temperature as the control parameter, whereas the pressure is less intensively investigated. In general, the anisotropy of strain by increasing pressure is very similar to cooling. The documented examples of pressure-induced ferroelectricity in metal complexes are very rare, with most of them as inorganic minerals.<sup>24,25</sup> The molecular framework compound  $\text{Zn}(\text{CN})_2$  is one of the few examples; it displays an improper first-order ferroelastic transition from the cubic structure to a denser orthorhombic structure at 1.52 GPa, and the rotations of connected pairs of  $\text{Zn}(\text{C}/\text{N})$  tetrahedra lead to an expansion of the crystallographic  $a$  axis.<sup>26</sup>

In this work, using high-pressure single-crystal X-ray diffraction together with *in situ* Raman spectroscopy, we show

Received: February 7, 2023

Accepted: April 12, 2023

Published: April 18, 2023



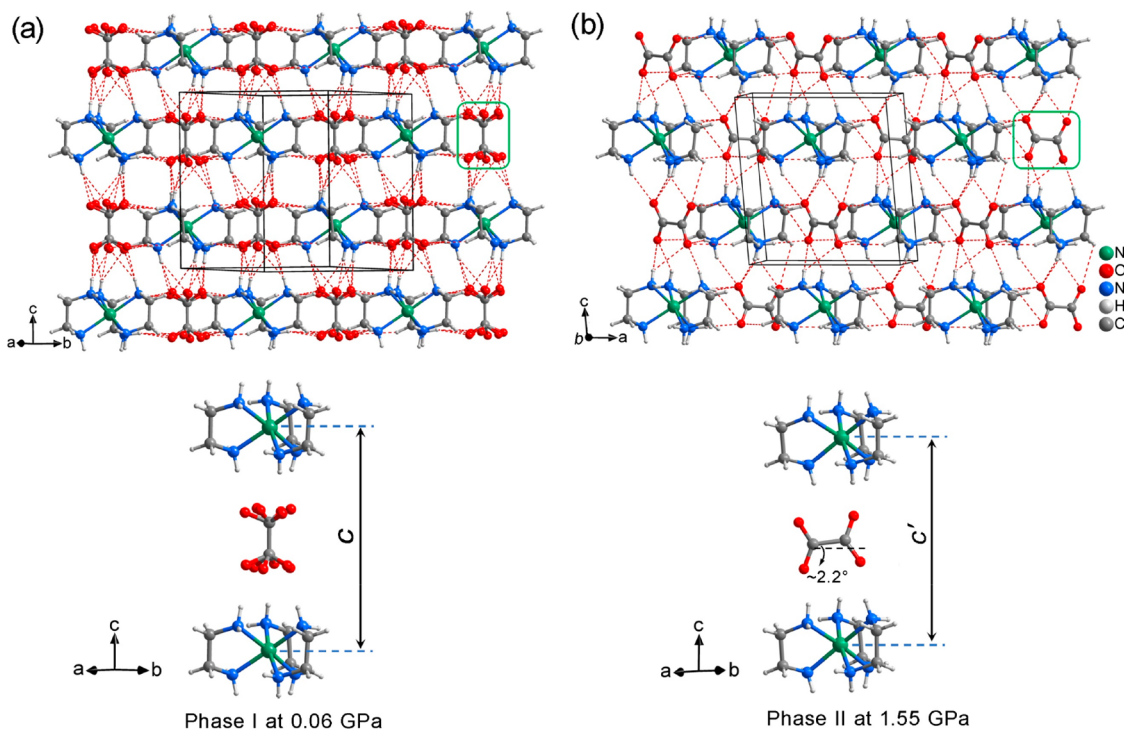


**Figure 1.** (a) Crystal structure of phase I of  $[\text{Ni}(\text{en})_3](\text{ox})$  at 0.06 GPa viewed approximately along the [110] direction. (b) Structure of phase II at 1.55 GPa. The red dashed lines represent  $\text{NH}\cdots\text{O}$  and  $\text{CH}\cdots\text{O}$  hydrogen bonds. The disordered oxalate anions in phase I, which convert to an ordered state in phase II with a rotation of  $90^\circ$ , are shown in the lower panels.

that the pressure induced a ferroelastic phase transition in a molecular crystal  $[\text{Ni}(\text{en})_3](\text{ox})$  ( $\text{en}$  = ethylenediamine and  $\text{ox}$  = oxalate anion) at a low pressure of  $\sim 0.2$  GPa with symmetry changing from trigonal  $P\bar{3}1c$  to monoclinic  $P2_1/n$ . The dynamically disordered oxalate anions transform to an ordered frozen structure with an unusual rotation of  $90^\circ$  through cooperative intermolecular interactions, resulting in a large shrinkage of the  $c$  axis during the ferroelastic transition, which can be clearly observed from the length change of the single crystal.

The light purple single crystals of  $[\text{Ni}(\text{en})_3](\text{ox})$  were grown by slow evaporation of an aqueous solution containing Ni(II) oxalate and ethylenediamine at room temperature as described previously.<sup>27</sup> At ambient conditions,  $[\text{Ni}(\text{en})_3](\text{ox})$  crystallizes in the trigonal symmetry with space group  $P\bar{3}1c$  ( $Z = 2$ ), denoted as phase I. Previous variable-temperature single-crystal X-ray diffraction measurements revealed that  $[\text{Ni}(\text{en})_3](\text{ox})$  undergoes a phase transition to the monoclinic  $P2_1/n$  structure (phase II) upon cooling at  $\sim 253$  K with the disorder-order transition of the oxalate anions, and such a transformation induced a large anisotropic shape change of 5%.<sup>22</sup> In the crystal structure of phase I, each  $\text{Ni}^{2+}$  cation adopts distorted octahedral geometry and is coordinated to six nitrogen atoms from three *en* ligands. The disordered  $\text{ox}^{2-}$  anions with a paddlewheel-like shape are parallel to the 3-fold rotation axis (*c* axis) and linked to the  $[\text{Ni}(\text{en})_3]^{2+}$  cations through  $\text{NH}\cdots\text{O}$  hydrogen bonds ( $\text{H}\cdots\text{O}$  distances range from 1.978 to 2.541 Å; see Figure 1a). Hence, from the crystal habit, the lattice parameter *c* axis should be parallel to the long axis of the rod-like pink single crystal.<sup>22</sup>

High-pressure single-crystal X-ray diffraction (SXRD) data of  $[\text{Ni}(\text{en})_3](\text{ox})$  were collected at room temperature up to 3.15 GPa (Table S1 of the Supporting Information). To ensure the hydrostatic environment, a 4:1 mixture of methanol–ethanol

(ME) was used as the pressure-transmitting medium (PTM).<sup>28</sup> In addition, synchrotron powder X-ray diffraction data were also recorded up to 15.2 GPa at room temperature using silicone oil as the PTM to investigate the effect of quasi-hydrostatic stress on the compressibility behavior of  $[\text{Ni}(\text{en})_3](\text{ox})$  (Figures S1 and S2 and Table S2 of the Supporting Information). As shown in Figure 2a, the lattice parameters of ambient-pressure phase I shrink monotonically up to  $\sim 0.20$  GPa, and above this pressure, a discontinuous transition to phase II was observed. Phase II crystallizes as the monoclinic space group  $P2_1/n$  ( $Z = 4$ ), which is isostructural to the phase observed below  $\sim 253$  K (upon cooling) at ambient pressure.<sup>22</sup> At ambient pressure (0.1 MPa), the thermal hysteresis width of the first-order phase transition of  $[\text{Ni}(\text{en})_3](\text{ox})$  is  $\sim 20$  K.<sup>22</sup> As a result of the uncertainty of the pressure measurement in the diamond anvil cell (DAC) chamber (0.03–0.05 GPa), it is not possible to accurately determine the transition pressure on the megapascal (MPa) scale during the decompression process. The phase transition pressure during decompression may be slightly different from that during compression. Therefore, we could not exclude the possibility of the existence of hysteresis according to the pressure-induced phase transition. This material requires further synchrotron X-ray experiments using a gas pressure cell (with tens of megapascal step) under variable pressure and temperature conditions to explore this possibility.

The symmetry elements of phase I ( $E$ ,  $3C_2$ ,  $2C_3$ ,  $2S_6$ ,  $i$ , and  $3\sigma_v$ ) changing to phase II ( $E$ ,  $C_2$ ,  $i$ , and  $\sigma_h$ ) can be described by the Aizu notation of  $\overline{3}mF2/m$ , among the 94 species of ferroelastic transitions.<sup>29</sup> At the transition pressure, the formula unit volume ( $V/Z$ ) drops by  $\sim 2.2\%$ , indicative of the first-order phase transition. Such a phase transformation is associated with the shrinkage of  $\sim 4.7\%$  of the lattice parameter  $c$  (positive compressibility; see Figure 2a). The large change in sub-

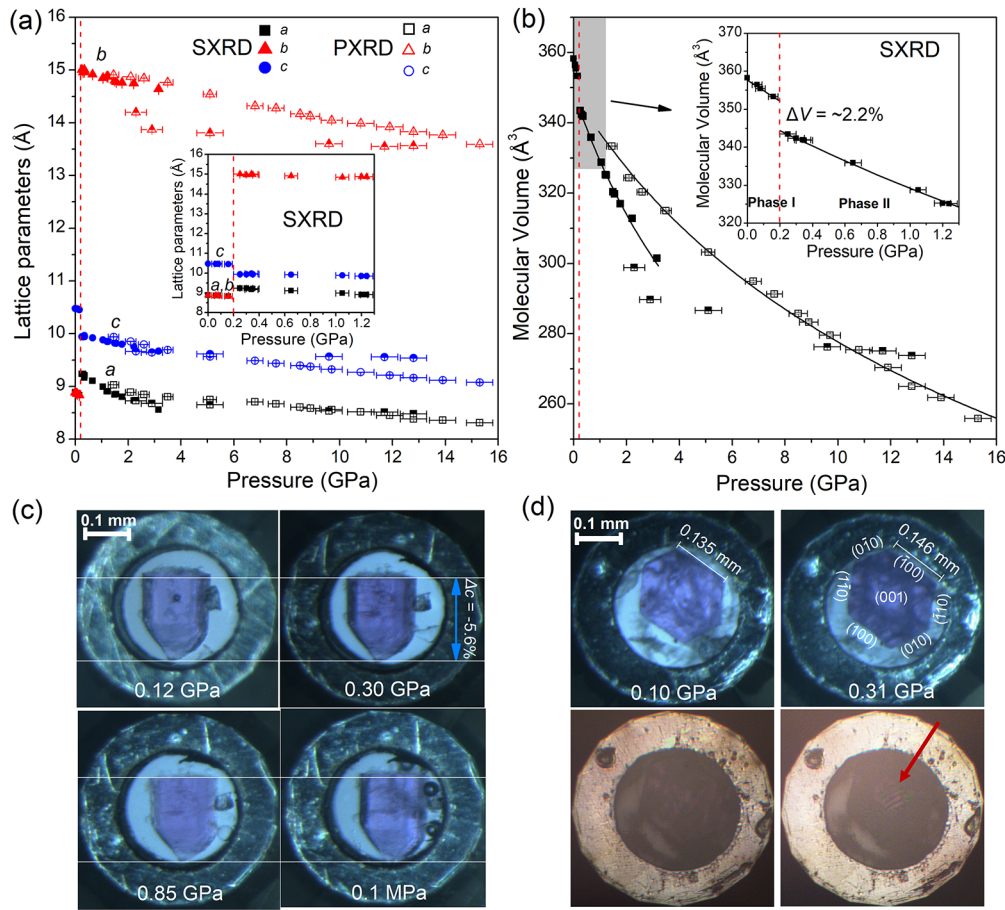


**Figure 2.** (a) Evolution of the lattice parameters of  $[\text{Ni}(\text{en})_3](\text{ox})$  with pressure. (b) Birch–Murnaghan equation of state fits to the formula unit volume ( $V/Z$ ) data. These lines are reference data for calculations of spontaneous strain and volume strain. The X-ray data collected from SXRD and PXRD are plotted as full and unfilled symbols, respectively. The half-filled symbols are PXRD data collected during the decompression process. The phase transition at  $\sim 0.20$  GPa is indicated by the red dashed line in both panels a and b. The insets highlight the changes of lattice parameters before and after phase transition. (c) Single crystal of  $[\text{Ni}(\text{en})_3](\text{ox})$  compressed in the ME mixture along the  $c$  axis. The length of the single crystal contracts from 0.231 mm (at 0.12 GPa) to 0.218 mm (at 0.30 GPa), and the crystal length could be fully recovered after the pressure released to 0.1 MPa (see the appearance of air bubbles). (d) Another single crystal was cut and loaded approximately along the  $ab$  plane. A few cotton fibers were used to stabilize the single crystal during pressurization. The bottom images show the polarized microscopy images at 0.10 and 0.31 GPa, respectively. The red arrow shows the appearance of diagonal stripes. The Miller indices of the crystal faces have been indicated in the upper panel.

nanometer size ( $\sim 0.5$  Å) caused by large rotational motions of the  $\text{ox}^{2-}$  anions can be directly reflected at the micrometer scale of the single crystal. As displayed in Figure 2c, we observed that the length shrinkage of the single crystal is about  $\sim 5.6\%$  between 0.12 and 0.3 GPa, which is comparable to the contraction rate of 5% at  $\sim 254$  K (0.1 MPa) during the phase transition.<sup>22</sup> The large linear compressibility [ $\sim 353(3)$  TPa<sup>-1</sup>] is more than 2 times larger than that of the flexible Zn-based metal–organic framework [ $145(9)$  TPa<sup>-1</sup>, caused by the negative area compressibility of puckered quadrangular rings within the  $ab$  plane].<sup>30</sup> After pressure was released from 0.85 GPa to ambient pressure, the length of the crystal could be fully recovered without crystal breaking, indicative of the reversible nature of the phase transition in the ME mixture. When silicone oil is used as the PTM, we assume that the shape change of the single crystal (ferroelastic transition) should be comparable to that in the ME mixture ( $\sim 0.2$  GPa), because the transition pressure is in the range of the hydrostatic limit of silicone oil ( $\sim 1.0$  GPa). When the pressure exceeds  $\sim 1.0$  GPa, different compression behaviors of the  $[\text{Ni}(\text{en})_3](\text{ox})$  complex were observed between silicone oil and the ME mixture as a result of the quasi-hydrostatic environment created in silicone oil (see panels a and b of Figure

2).<sup>31</sup> After the pressure exceeds 1.0 GPa, the deviatoric stress generated by the quasi-hydrostatic environment causes the powder X-ray diffraction patterns to become broader. As shown in Figure S1 of the Supporting Information, the  $[\text{Ni}(\text{en})_3](\text{ox})$  sample may partially lose its crystallinity after the pressure reaches 15.3 GPa, which is evidenced by the lattice parameters from the decompression X-ray data that could not be fully recovered (see panels a and b of Figure 2). As shown in Figure 2d, clear stripe-shaped domains appeared at the  $ab$  plane at 0.31 GPa (phase II) under the polarized microscope, providing solid experimental evidence of ferroelasticity. The magnitude of the linear compressibility of the lattice parameter  $a(b)$  axis is  $33.4(6)$  TPa<sup>-1</sup>, while the  $c$  axis is more robust, with a magnitude of  $14.7(5)$  TPa<sup>-1</sup> from 0.1 MPa to 0.16 GPa throughout the phase I region. When the pressure is increased to 3.15 GPa in phase II, all of the lattice parameters  $a$ ,  $b$ , and  $c$  show positive linear compressibility (PLC). The magnitude of the strain tensor eigenvector  $\beta_3$  of  $9.3(5)$  TPa<sup>-1</sup> is inclined by  $12.6^\circ$  to the  $c$  axis, which is comparable to that along the  $b$  axis [ $\beta_b = 9.1(16)$  TPa<sup>-1</sup>]. The strongest PLC is approximately along the  $a$  axis (inclined by  $14.2^\circ$ ), and the corresponding coefficient  $\beta_1$  is equal to  $28.2(23)$  TPa<sup>-1</sup>, which is about 3 times that of  $\beta_b$  (see Table

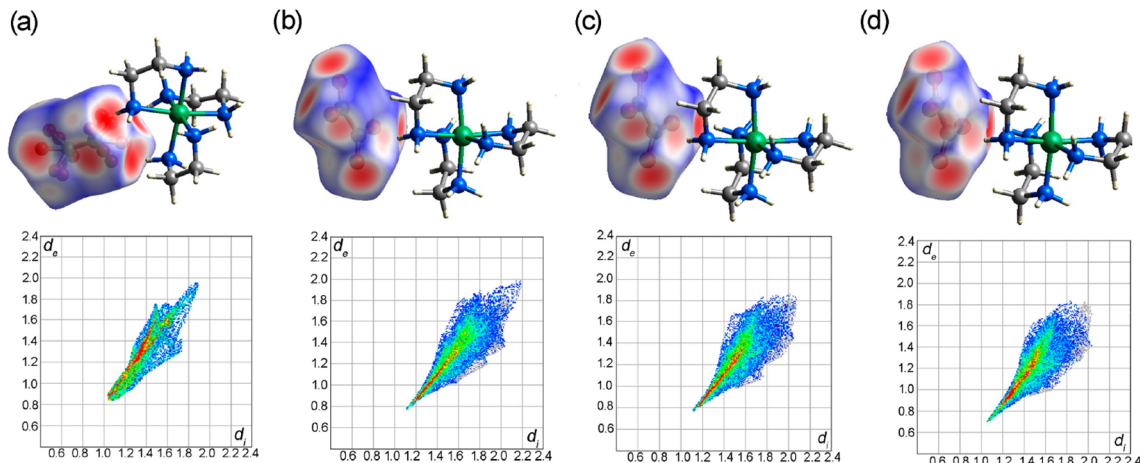


**Figure 3.** Hirshfeld surfaces of ox<sup>2-</sup> anions in (a) phase I at 0.16 GPa, (b) phase II at 0.35 GPa, (c) 1.55 GPa, and (d) 3.15 GPa. The color scale describes distances longer (navy blue), equal (white), and shorter (red) than the van der Waals radii. The corresponding 2D fingerprint plots of H···O are shown in the bottom panel.

S3 of the Supporting Information). The  $\beta$  angle increases by about 1.0° to  $\sim$ 3.0 GPa and then decreases slightly by  $\sim$ 0.8% as the pressure is increased to 15.2 GPa (Figure S3 of the Supporting Information).

According to  $-3mF2/m$  of the Aizu notation, the magnitude of the total spontaneous strain  $\varepsilon_{ss}$  of [Ni(en)<sub>3</sub>](ox) is given as  $\varepsilon_{ss} = (2w^2 + 2\varepsilon_{12}^2 + 2\varepsilon_{13}^2 + 2\varepsilon_{23}^2)^{1/2}$ , where  $w = 0.5(\varepsilon_{22} - \varepsilon_{11})$ .<sup>5,32</sup> The calculated total spontaneous strain  $\varepsilon_{ss}$  is equal to 0.784 (see the Supporting Information for specific details). The volume strain  $V_s$  is defined as  $V_s = (V - V_0)/V_0$ , where  $V$  is the molecular volume of the low-symmetry phase II ( $P2_1/n$ ) and  $V_0$  is the high-symmetry phase I ( $P\bar{3}1c$ ) at the transition pressure of  $\sim$ 0.2 GPa. From the extrapolation by equations of state of both phases, the calculated volume strain  $V_s$  is  $-2.12\%$ , which is more than 10 times larger than that of the prototypic mineral Pb<sub>3</sub>(PO<sub>4</sub>)<sub>2</sub> ( $-0.13\%$ )<sup>33</sup> but about 40% of the magnitude of the molecular framework Zn(CN)<sub>2</sub> ( $-5.44\%$ ).<sup>26</sup> The significant difference in the volume strain between [Ni(en)<sub>3</sub>](ox) and Zn(CN)<sub>2</sub> during the ferroelastic transition is most likely due to the hydrogen-bonding constraints of the rotational motions of the ox<sup>2-</sup> anions during the symmetry breaking in [Ni(en)<sub>3</sub>](ox). In contrast, only rotations of connected Zn(C/N) tetrahedra occur in the molecular framework Zn(CN)<sub>2</sub>.<sup>26</sup>

The unit cell volume of phase I can be well-fitted to the second-order Birch–Murnaghan equation of state with the zero-pressure bulk modulus  $B_0$  of 12.4(16) GPa and its pressure derivative  $B'$  fixed at 4, revealing the soft nature of the [Ni(en)<sub>3</sub>](ox) crystal, which resembles most organic molecular crystals.<sup>34</sup> In phase II, the second-order Birch–Murnaghan equation of state gives  $B_0$  of 15.6(5) GPa and  $B'$  of 4, which shows that phase II is slightly harder than phase I. However, in our powder X-ray diffraction (PXRD) measurements using silicone oil as the PTM, the second-order Birch–Murnaghan equation of state demonstrates  $B_0$  of 27.9(9) GPa with  $B'$  of 4.0 in phase II, which is almost 2 times larger than that in the PTM of the ME mixture, implying that the [Ni(en)<sub>3</sub>](ox) single crystal is extremely sensitive to the hydrostatic environment. Such character has been observed in most of the soft materials, such as coordination polymers<sup>35,36</sup> and hybrid perovskites.<sup>37–39</sup>

In the monoclinic high-pressure phase II, the trigonal symmetry is broken, the oxygen atoms of the ox<sup>2-</sup> anions are crystallographically ordered, and the whole anions undergo

significant rotation of 90° in accordance with the  $c$  axis, whereas the packing arrangements of the [Ni(en)<sub>3</sub>]<sup>2+</sup> cations are hardly modified (Figure 1b). The C–C bonds within the ox<sup>2-</sup> anions are approximately parallel to the  $ab$  plane, with a slight deviation angle of  $\sim$ 2.2° (Figure 1b). The main difference between phases I and II is that the ox<sup>2-</sup> anions transform from a “standing up” to “lying down” position and give rise to new CH···O hydrogen bonds (Figure 1 and Table S4 of the Supporting Information).<sup>22</sup> In contrast to the temperature, the external hydrostatic pressure triggers large systematic responses in the phase II structure. For example, the ox<sup>2-</sup> anions possess a nonplanar conformation, and their torsion angles of O2–C7–C8–O3 and O1–C7–C8–O4 are 171.8(18)° and 168.2(17)° at 0.35 GPa, respectively, and these magnitudes gradually decrease under compression (Figure S4 of the Supporting Information). Such conformational changes are most likely arising from the enhanced directional NH···O and CH···O hydrogen bonds under compression. In the [Ni(en)<sub>3</sub>]<sup>2+</sup> cations of phase II, the Ni–N bond lengths demonstrate a subtle reduction under compression. For example, the Ni1–N2 bond distances decrease slightly from 2.14(1) Å (at 0.35 GPa) to 2.08(2) Å (at 3.15 GPa) (see Figure S5 of the Supporting Information). The NH···O and CH···O intermolecular interactions of phase II are gradually reduced with increasing the pressure (Table S4 of the Supporting Information). The changes of intermolecular contacts during the ferroelastic transition from phase I to phase II can be clearly illustrated from the differences of Hirshfeld surfaces and two-dimensional (2D) fingerprint plots (Figure 3).<sup>40</sup> The disordered–ordered and orientational changes of ox<sup>2-</sup> anions yield different Hirshfeld surfaces. In phase I, the disordered ox<sup>2-</sup> anions generate large red spots around the oxygen atoms, indicative of strong H···O bonding (Figure 3a). In phase II, the H···O contacts became shorter under compression, which is characterized by larger red spots on the Hirshfeld surfaces at 3.15 GPa (panels b–d of Figure 3). In contrast to the large reductions of H···O interactions in organic molecular crystals under pressure,<sup>41</sup> the relative contributions of H···O contacts in phase II reduce subtly under compression, *i.e.*, 89% (0.35 GPa) versus 88% (3.15 GPa).

The ferroelastic phase transition was further confirmed by *in situ* high-pressure Raman spectroscopy. Figure 4 shows the pressure-dependent Raman spectra of [Ni(en)<sub>3</sub>](ox) using the

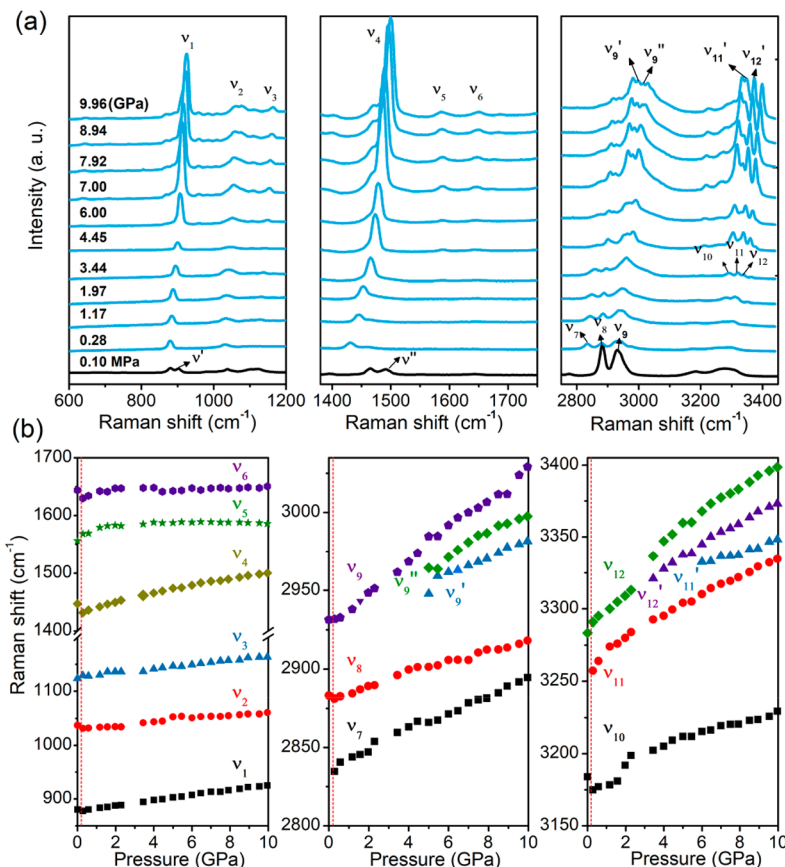


**Figure 4.** (a) Selected Raman spectra of  $[\text{Ni}(\text{en})_3](\text{ox})$  upon compression to  $\sim 10.0$  GPa and (b) evolution of Raman modes during compression.

ME mixture as the PTM. When the pressure increased to 0.28 GPa, the Raman spectra of the sample exhibit substantial changes, demonstrating the occurrence of the phase transition (Figure S6 of the Supporting Information). For example, the modes  $\nu_4$  ( $1446.7 \text{ cm}^{-1}$ ,  $\text{CH}_2$  bending) and  $\nu_{10}$  ( $3184.0 \text{ cm}^{-1}$ ,  $\text{NH}_2$  stretching) from the *en* ligand at 0.1 MPa show blue shifts to  $1431.7$  and  $3172.6 \text{ cm}^{-1}$  at 0.28 GPa, respectively (Figure S6 and Table S5 of the Supporting Information). These features indicate that the breakage and reconstruction of hydrogen bonding (rotation of oxalate anions) slightly alter the conformations of the *en* ligands during the phase transition. Meanwhile, a large red shift of the  $\nu_5$  band ( $\text{C}=\text{O}$  stretching mode) with magnitude of  $\sim 12 \text{ cm}^{-1}$  was observed with the pressure increased from 0.1 MPa to 0.28 GPa, revealing the modifications of the vibrations of the  $\text{ox}^{2-}$  anions. Such character is well-consistent with the disorder-order transition of the  $\text{ox}^{2-}$  anions as revealed by the single-crystal X-ray diffraction. In the high-pressure phase II, all of the bands show a red shift under compression, and the symmetric  $\text{NH}_2$  stretching  $\nu_{12}$  band displays the largest  $d\nu/dp$  coefficient ( $11.50 \text{ cm}^{-1}/\text{GPa}$ ), which is almost 6 times larger than of the  $\text{NH}_2$  bending mode  $\nu_6$  ( $2.03 \text{ cm}^{-1}/\text{GPa}$ ). Moreover, some bands split into doublets or triplets at 5.0 GPa; e.g., the  $\nu_9$  band ( $\text{CH}_2$  symmetric stretching) at  $2984.6 \text{ cm}^{-1}$  splits into  $2947.8$  and  $2964.4 \text{ cm}^{-1}$  doublets, respectively (Figure 4b). The splitting and appearance of the new modes demonstrate the low-symmetry structure and enhanced directional hydrogen bonding under pressurization.

In summary, we report that dynamically disordered single-crystal  $[\text{Ni}(\text{en})_3](\text{ox})$  undergoes a ferroelastic transition with a large shape change in response to the external hydrostatic

pressure of  $\sim 0.2$  GPa. Systematic structural analyses reveal that the disorder-order transformation and uncommon rotation of  $90^\circ$  of  $\text{ox}^{2-}$  anions via cooperative intermolecular hydrogen bonding are responsible for the abnormally large contraction rate of the single crystal. Furthermore, the ferroelastic transition from high-symmetry  $P\bar{3}1c$  to low-symmetry  $P2_1/n$  was systematically studied by X-ray diffraction and Raman spectroscopy as well as Hirshfeld surface analyses. This study provides a new approach for triggering a pronounced shape change of the single crystal by modulating the orientations of the components of the crystal under pressure. Such a concept could be applied to other molecular crystals for designing and developing potentially new functional piezo-responsive hybrid materials with exceptional physical properties.

## ASSOCIATED CONTENT

### Supporting Information

The Supporting Information is available free of charge at <https://pubs.acs.org/doi/10.1021/acs.jpcllett.3c00356>.

Experimental methods and spontaneous strain calculations, PXRD patterns and selective Le Bail refinements, structure information on phases I and II of  $[\text{Ni}(\text{en})_3](\text{ox})$  as a function of the pressure, assignment of Raman spectra of phases I and II of  $[\text{Ni}(\text{en})_3](\text{ox})$  at different pressures, crystal data, refinement parameters, and intermolecular hydrogen bonds (PDF)

X-ray crystallographic data for phase I at 0.1 MPa and 0.06 and 0.16 GPa (CIF)

X-ray crystallographic data for phase II at 0.35, 1.55, 1.77, 2.21, and 3.15 GPa (CIF)

## AUTHOR INFORMATION

### Corresponding Authors

**Wei Li** – School of Materials Science and Engineering, Nankai University, Tianjin 300350, People's Republic of China;  [orcid.org/0000-0002-5277-6850](https://orcid.org/0000-0002-5277-6850); Email: [wli276@nankai.edu.cn](mailto:wli276@nankai.edu.cn)

**Weizhao Cai** – School of Materials and Energy, University of Electronic Science and Technology of China, Chengdu, Sichuan 611731, People's Republic of China;  [orcid.org/0000-0001-7805-2108](https://orcid.org/0000-0001-7805-2108); Email: [wzhcai@uestc.edu.cn](mailto:wzhcai@uestc.edu.cn)

### Authors

**Boyang Fu** – School of Materials and Energy, University of Electronic Science and Technology of China, Chengdu, Sichuan 611731, People's Republic of China

**Ying Zhao** – School of Materials Science and Engineering, Nankai University, Tianjin 300350, People's Republic of China

**Yu Liu** – School of Materials and Energy, University of Electronic Science and Technology of China, Chengdu, Sichuan 611731, People's Republic of China

**Weilong He** – School of Materials and Energy, University of Electronic Science and Technology of China, Chengdu, Sichuan 611731, People's Republic of China

**Fuyang Liu** – Center for High Pressure Science and Technology Advanced Research, Beijing 100094, People's Republic of China

**Dongzhou Zhang** – PX2, Hawaii Institute of Geophysics and Planetology, University of Hawaii at Manoa, Honolulu, Hawaii 96822, United States;  [orcid.org/0000-0002-6679-892X](https://orcid.org/0000-0002-6679-892X)

**Luhong Wang** – Department of Geology, University of Illinois Urbana–Champaign, Urbana, Illinois 61801, United States; Shanghai Advanced Research in Physical Sciences, Shanghai 201203, People's Republic of China

**Haozhe Liu** – Center for High Pressure Science and Technology Advanced Research, Beijing 100094, People's Republic of China

Complete contact information is available at:

<https://pubs.acs.org/10.1021/acs.jpcllett.3c00356>

### Notes

The authors declare no competing financial interest.

## ACKNOWLEDGMENTS

This work was financially supported by the National Natural Science Foundation of China (12274062) and the National Science Foundation of Sichuan Province (2022NSFSC0297). Portions of this work were performed at GeoSoilEnviroCARS (The University of Chicago), Advanced Photon Source (APS), Argonne National Laboratory. GeoSoilEnviroCARS is supported by the National Science Foundation—Earth Sciences (EAR-1634415) and Department of Energy—GeoSciences (DE-FG02-94ER14466). This research used resources of the APS, a U.S. Department of Energy (DOE) Office of Science User Facility operated for the DOE Office of Science by Argonne National Laboratory, under Contract DE-AC02-06CH11357.

## REFERENCES

- (1) Salje, E. K. H. Ferroelastic Materials. *Annu. Rev. Mater. Res.* **2012**, *42*, 265–283.

(2) Hu, Y.; You, L.; Xu, B.; Li, T.; Morris, S. A.; Li, Y.; Zhang, Y.; Wang, X.; Lee, P. S.; Fan, H. J.; Wang, J. Ferroelastic-Switching-Driven Large Shear Strain and Piezoelectricity in a Hybrid Ferroelectric. *Nat. Mater.* **2021**, *20*, 612–617.

(3) Aizu, K. Possible Species of Ferromagnetic, Ferroelectric, and Ferroelastic Crystals. *Phys. Rev. B* **1970**, *2*, 754–772.

(4) Wadhawan, V. K. Ferroelasticity. *Bull. Mater. Sci.* **1984**, *6*, 733–753.

(5) Carpenter, M. A.; Salje, E. K. H.; Graeme-Barber, A. Spontaneous Strain as a Determinant of Thermodynamic Properties for Phase Transitions in Minerals. *Eur. J. Mineral.* **1998**, *10*, 621–691.

(6) Worlton, T. G.; Beyerlein, R. A. Structure and Order Parameters in the Pressure-Induced Continuous Transition in  $\text{TeO}_2$ . *Phys. Rev. B* **1975**, *12*, 1899–1907.

(7) Cairns, A. B.; Goodwin, A. L. Negative Linear Compressibility. *Phys. Chem. Chem. Phys.* **2015**, *17*, 20449–20465.

(8) Uwe, H.; Tokumoto, H. Pressure-Induced Ferroelastic Transition and Internal Displacement in  $\text{TeO}_2$ . *Phys. Rev. B* **1979**, *19*, 3700–3707.

(9) Angel, R. J.; Bismayer, U. Renormalization of the Phase Transition in Lead Phosphate,  $\text{Pb}_3(\text{PO}_4)_2$ , by High Pressure: Lattice Parameters and Spontaneous Strain. *Acta Crystallogr., Sect. B: Struct. Sci.* **1999**, *55*, 896–901.

(10) Angel, R. J.; Bismayer, U.; Marshall, W. G. Renormalization of the Phase Transition in Lead Phosphate,  $\text{Pb}_3(\text{PO}_4)_2$ , by High Pressure: Structure. *J. Phys.: Condens. Matter* **2001**, *13*, 5353–5364.

(11) Xu, W.-J.; Zeng, Y.; Yuan, W.; Zhang, W.-X.; Chen, X.-M. A Large Room-Temperature Entropy Change in a New Hybrid Ferroelastic with an Unconventional Bond-Switching Mechanism. *Chem. Commun.* **2020**, *56*, 10054–10057.

(12) Liu, D.-X.; Chen, X.-X.; Ye, Z.-M.; Zhang, W.-X.; Chen, X.-M. High- and Low-Temperature Dual Ferroelasticity in a New Hybrid Crystal:  $(\text{Me}_3\text{NCH}_2\text{CH}_2\text{OH})_4[\text{Ni}(\text{NCS})_6]$ . *Sci. China Mater.* **2022**, *65*, 263–267.

(13) Huang, P.-Z.; Ni, H.-F.; Su, C.-Y.; Lun, M.-M.; Lu, H.-F.; Fu, D.-W.; Guo, Q. Thermal-Induced Ferroelastics in Two Lead-free Organic-Inorganic Hybrid Perovskites. *CCS Chem.* **2022**, *1*, 1–10.

(14) Zhang, H.-Y.; Hu, C.-L.; Hu, Z.-B.; Mao, J.-G.; Song, Y.; Xiong, R.-G. Narrow Band Gap Observed in a Molecular Ferroelastic: Ferrocenium Tetrachloroferrate. *J. Am. Chem. Soc.* **2020**, *142*, 3240–3245.

(15) Zeng, Y.-L.; Ai, Y.; Tang, S.-Y.; Song, X.-J.; Chen, X.-G.; Tang, Y.-Y.; Zhang, Z.-X.; You, Y.-M.; Xiong, R.-G.; Zhang, H.-Y. Axial-Chiral BINOL Multiferroic Crystals with Coexistence of Ferroelectricity and Ferroelasticity. *J. Am. Chem. Soc.* **2022**, *144*, 19559–19566.

(16) Maughan, A. E.; Mozur, E. M.; Candia, A. M.; Neilson, J. R. Ferroelastic Phase Transition in Formamidinium Tin(IV) Iodide Driven by Organic-Inorganic Coupling. *Inorg. Chem.* **2020**, *59*, 14399–14406.

(17) Liu, Z.-B.; He, L.; Shi, P.-P.; Ye, Q.; Fu, D.-W. A Three-Dimensional Molecular Perovskite Ferroelastic with Two-Step Switching of Quadratic Nonlinear Optical Properties Tuned by Molecular Chiral Design. *J. Phys. Chem. Lett.* **2020**, *11*, 7960–7965.

(18) Li, K.; Li, Z.-G.; Xu, J.; Qin, Y.; Li, W.; Stroppa, A.; Butler, K. T.; Howard, C. J.; Dove, M. T.; Cheetham, A. K.; Bu, X.-H. Origin of Ferroelectricity in Two Prototypical Hybrid Organic-Inorganic Perovskites. *J. Am. Chem. Soc.* **2022**, *144*, 816–823.

(19) Li, W.; Zhang, Z.; Bithell, E. G.; Batsanov, A. S.; Barton, P. T.; Saines, P. J.; Jain, P.; Howard, C. J.; Carpenter, M. A.; Cheetham, A. K. Ferroelasticity in a Metal–Organic Framework Perovskite; Towards a New Class of Multiferroics. *Acta Mater.* **2013**, *61*, 4928–4938.

(20) Szklarz, P.; Jakubas, R.; Medycki, W.; Gągor, A.; Cichos, J.; Karbowiak, M.; Bator, G.  $(\text{C}_3\text{N}_2\text{H}_5)_3\text{Sb}_2\text{I}_9$  and  $(\text{C}_3\text{N}_2\text{H}_5)_3\text{Bi}_2\text{I}_9$ : Ferroelastic Lead-Free Hybrid Perovskite-Like Materials as Potential Semiconducting Absorbers. *Dalton Trans.* **2022**, *51*, 1850–1860.

(21) Rok, M.; Moskwa, M.; Działowa, M.; Bieńko, A.; Rajnák, C.; Boća, R.; Bator, G. Multifunctional Materials Based on the Double-Perovskite Organic-Inorganic Hybrid  $(\text{CH}_3\text{NH}_3)_2[\text{KCr}(\text{CN})_6]$  Showing Switchable Dielectric, Magnetic, and Semiconducting Behaviour. *Dalton Trans.* **2019**, *48*, 16650–16660.

- (22) Yao, Z.-S.; Mito, M.; Kamachi, T.; Shiota, Y.; Yoshizawa, K.; Azuma, N.; Miyazaki, Y.; Takahashi, K.; Zhang, K.; Nakanishi, T.; Kang, S.; Kanegawa, S.; Sato, O. Molecular Motor-Driven Abrupt Anisotropic Shape Change in a Single Crystal of a Ni Complex. *Nat. Chem.* **2014**, *6*, 1079–1083.
- (23) Yuan, W.; Zeng, Y.; Tan, Y.-Y.; Zhou, J.-H.; Xu, W.-J.; Zhang, W.-X.; Chen, X.-M. A New Ferroelastic Hybrid Material with a Large Spontaneous Strain:  $(\text{Me}_3\text{NOH})_2[\text{ZnCl}_4]$ . *Chem. Commun.* **2019**, *55*, 8983–8986.
- (24) Gregoryanz, E.; Hemley, R. J.; Mao, H.-K.; Gillet, P. High-Pressure Elasticity of  $\alpha$ -Quartz: Instability and Ferroelastic Transition. *Phys. Rev. Lett.* **2000**, *84*, 3117–3120.
- (25) Zhang, Y.; Fu, S.; Wang, B.; Lin, J.-F. Elasticity of a Pseudoproper Ferroelastic Transition from Stishovite to Post-Stishovite at High Pressure. *Phys. Rev. Lett.* **2021**, *126*, 025701.
- (26) Collings, I. E.; Cairns, A. B.; Thompson, A. L.; Parker, J. E.; Tang, C. C.; Tucker, M. G.; Catafesta, J.; Levelut, C.; Haines, J.; Dmitriev, V.; Pattison, P.; Goodwin, A. L. Homologous Critical Behavior in the Molecular Frameworks  $\text{Zn}(\text{CN})_2$  and  $\text{Cd}(\text{imidazolate})_2$ . *J. Am. Chem. Soc.* **2013**, *135*, 7610–7620.
- (27) Padmanabhan, M.; Joseph, J. C.; Huang, X.; Li, J. Diamine Incorporated Compounds Derived from Polymeric Nickel(II) Fumarates and Oxalates: Crystal Structure, Spectral and Thermal Properties of  $[\text{Ni}(\text{en})_3](\text{O}_2\text{CCHCHCO}_2)_2 \cdot 3\text{H}_2\text{O}$  and  $[\text{Ni}(\text{en})_3](\text{O}_2\text{CCO}_2)_2$ . *J. Mol. Struct.* **2008**, *885*, 36–44.
- (28) Klotz, S.; Chervin, J. C.; Munsch, P.; Le Marchand, G. Hydrostatic Limits of 11 Pressure Transmitting Media. *J. Phys. D: Appl. Phys.* **2009**, *42*, 075413.
- (29) Aizu, K. Possible Species of “Ferroelastic” Crystals and of Simultaneously Ferroelectric and Ferroelastic Crystals. *J. Phys. Soc. Jpn.* **1969**, *27*, 387–396.
- (30) Cai, W.; Gladysiak, A.; Aniola, M.; Smith, V. J.; Barbour, L. J.; Katrusiak, A. Giant Negative Area Compressibility Tunable in a Soft Porous Framework Material. *J. Am. Chem. Soc.* **2015**, *137*, 9296–9301.
- (31) Angel, R. J.; Bujak, M.; Zhao, J.; Gatta, G. D.; Jacobsen, S. D. Effective Hydrostatic Limits of Pressure Media for High-Pressure Crystallographic Studies. *J. Appl. Crystallogr.* **2007**, *40*, 26–32.
- (32) Aizu, K. Determination of the State Parameters and Formulation of Spontaneous Strain for Ferroelastics. *J. Phys. Soc. Jpn.* **1970**, *28*, 706–716.
- (33) Angel, R. J.; Bismayer, U.; Marshall, W. G. Local and Long-Range Order in Ferroelastic Lead Phosphate at High Pressure. *Acta Crystallogr., Sect. B: Struct. Sci.* **2004**, *60*, 1–9.
- (34) Safari, F.; Katrusiak, A. High-Pressure Polymorphs Nucleated and Stabilized by Rational Doping under Ambient Conditions. *J. Phys. Chem. C* **2021**, *125*, 23501–23509.
- (35) Andrzejewski, M.; Katrusiak, A. Piezochromic Topology Switch in a Coordination Polymer. *J. Phys. Chem. Lett.* **2017**, *8*, 929–935.
- (36) Sobczak, S.; Roszak, K.; Katrusiak, A. Exchanged Metal-Hydrogen Anagostic Bonds and Resonance of Dithiocarbamate and Thioureide Mesomers. *Chem. - Eur. J.* **2022**, *28*, e202201235.
- (37) Zhang, R.; Cai, W.; Bi, T.; Zarifi, N.; Terpstra, T.; Zhang, C.; Verdeny, Z. V.; Zurek, E.; Deemyad, S. Effects of Nonhydrostatic Stress on Structural and Optoelectronic Properties of Methylammonium Lead Bromide Perovskite. *J. Phys. Chem. Lett.* **2017**, *8*, 3457–3465.
- (38) Szafrański, M.; Katrusiak, A. Photovoltaic Hybrid Perovskites under Pressure. *J. Phys. Chem. Lett.* **2017**, *8*, 2496–2506.
- (39) Maczka, M.; Sobczak, S.; Ratajczyk, P.; Leite, F. F.; Paraguassu, W.; Dybala, F.; Herman, A. P.; Kudrawiec, R.; Katrusiak, A. Pressure-Driven Phase Transition in Two-Dimensional Perovskite  $\text{MH}_2\text{PbBr}_4$ . *Chem. Mater.* **2022**, *34*, 7867–7877.
- (40) Spackman, M. A.; Jayatilaka, D. Hirshfeld Surface Analysis. *CrystEngComm* **2009**, *11*, 19–32.
- (41) Cai, W.; Marciak, J.; Andrzejewski, M.; Katrusiak, A. Pressure Effect on D,L-Mandelic Acid Racemate Crystallization. *J. Phys. Chem. C* **2013**, *117*, 7279–7285.

## □ Recommended by ACS

### Thickness-Dependent Interface Polarity in Infinite-Layer Nickelate Superlattices

Chao Yang, Peter A. van Aken, et al.

APRIL 07, 2023

NANO LETTERS

READ ▶

### Intercalating Helium into A-Site Vacant Perovskites

Stefano Racioppi, Eva Zurek, et al.

MAY 23, 2023

CHEMISTRY OF MATERIALS

READ ▶

### High-Pressure Diffusion Control: Na Extraction from $\text{NaAlB}_{14}$

Masaya Fujioka, Junji Nishii, et al.

MARCH 21, 2023

CHEMISTRY OF MATERIALS

READ ▶

### Crystal Growth and Phase Formation of High-Entropy Rare-Earth Aluminum Perovskites

Matheus Pianassola, Mariya Zhuravleva, et al.

DECEMBER 09, 2022

CRYSTAL GROWTH & DESIGN

READ ▶

Get More Suggestions >